Research Article

Yahu Song, Aiqin Wang*, Douqin Ma, Jingpei Xie, and Wenyan Wang

Dynamic recrystallization behavior and nucleation mechanism of dual-scale $SiC_p/A356$ composites processed by P/M method

https://doi.org/10.1515/ntrev-2022-0506 received May 22, 2022; accepted January 2, 2023

Abstract: Thermal deformation can improve the properties of aluminum matrix composites (AMCs) prepared by powder metallurgy (P/M) due to the dense and uniform microstructures. And the final microstructure of the AMCs is related to the dynamic recrystallization (DRX) behavior and nucleation mechanism in the thermal forming process. In this regard, the hot compression tests of dual-scale SiC particles reinforced A356 (SiC_p/A356) composites prepared by P/M method were carried out at temperatures of 460–520°C and strain rates of 0.01–5 s⁻¹ on a thermal simulation tester. The corresponding microstructure evolution was analyzed by electron back-scattered diffraction and transmission electron microscopy. The results indicated that the stress-strain curve was a typical DRX unimodal stress curve. The comprehensive influences of the strain rate and deformation temperature on the stress were investigated using the Zener-Hollomon parameter (Z), where the deformation activation energy was 443.204 kJ/mol. The DRX critical strain model and DRX volume fraction model were established. DRX behavior of the SiC_p/A356 composites was sensitive to the deformation temperatures and strain rates. The micro and nano SiC_p can promote the DRX nucleation of Al matrix due to the particle-stimulated nucleation.

Keywords: dual-scale, SiC_p/A356 composites, dynamic recrystallization, nucleation mechanism

1 Introduction

Aluminum matrix composites (AMCs) reinforced by particles are wildly used in aerospace, national defense industry, automobile industry, electronic packaging, and other hightech fields due to their excellent mechanical and physical properties [1–3]. Generally, the properties of the AMCs may be improved by adding a single micron or nanoparticle as the reinforcing phase. The research shows that micron particle significantly enhances the strength, hardness, and wear resistance of AMCs, while leading to a sharp decline in their plasticity and toughness [4,5]. For the nanoparticles, they have apparent size effects, which can enhance the strength, plasticity, and toughness of AMCs. However, the AMCs reinforced by high-volume fraction nanoparticles are challenging to prepare due to the easy agglomerate of nanoparticles, which significantly limits the application [6,7]. However, more attention has been paid to developing micron and nanoparticle hybrid aluminum matrix composites (HAMCs) with good comprehensive properties due to the different strengthening mechanisms of the reinforcements [8–10]. Zhang et al. [8] have investigated the effects of SiC_p with varying scales on the microstructure and properties of Al2014 composites. The research shows that compared with Al2014 alloy, micron SiC_p composite and nano SiC_p composite, and dual-scale SiC_p/Al2014 composites present more excellent mechanical properties. The creep resistance of the different-sized TiC_p/Al-Cu composites has been studied by Tian et al. [9]. Their results demonstrate that the creep resistance of the dual-scale (micron + nano) TiC_p/Al-Cu composite is 10–38 times and 3–6 times higher than that of the Al-Cu matrix alloy and single-scale composites, respectively.

To improve the performance of AMCs prepared by powder metallurgy (P/M), further processing, such as

^{*} Corresponding author: Aiqin Wang, School of Materials Science and Engineering, Henan University of Science and Technology, Luoyang 471023, China, e-mail: aiqin_wang888@163.com Yahu Song: School of Materials Science and Engineering, Henan University of Science and Technology, Luoyang 471023, China; CITIC Heavy Industries Co., Ltd, Luoyang 471039, Henan, China Douqin Ma, Jingpei Xie, Wenyan Wang: School of Materials Science and Engineering, Henan University of Science and Technology, Luoyang 471023, China; Provincial and Ministerial Co-construction of Collaborative Innovation Center of Non-ferrous Metals New Materials and Advanced Processing Technology, Henan University of Science and Technology, Luoyang, 471023, China

hot extrusion, forging, and rolling, should be proceeded to obtain the dense and uniform microstructure. However, the hot workability of AMCs is usually poor due to the difference in hardness and thermal expansion coefficient between the particles and the Al matrix [11,12]. Researchers have revealed that dynamic recrystallization (DRX) behavior is advantageous to the refinement and homogenization of the grain in AMCs, which is a crucial deformation mechanism to reconstitute the microstructure and enhance its properties during the hot working process [13,14]. Therefore, it is significant to research the DRX behavior of HAMCs during hot deformation to improve the microstructure and enhance the properties.

Presently, it is commonly accepted that the addition of reinforcement particles has an essential effect on the DRX behavior of aluminum matrix. When the particle size is greater than 1 µm, due to the mismatch between the deformation of the particle and matrix, the deformation zone with high dislocation density and orientation gradient will be formed near the particle, which can promote the nucleation of DRX. This is called particle-stimulated nucleation (PSN) [15,16]. As the particle size is less than 1 µm, the small-scale particles have a strong pinning effect on the grain boundaries, delaying the recrystallization process and inhibiting the recrystallization nucleation to a certain extent [17]. However, the research on AMCs by Zhao et al. [18] and Kai et al. [19] shows that nanoparticles can promote the nucleation of DRX. Meanwhile, Radi and Mahmudi [20] also obtained the same results in nanoparticle-reinforced magnesium matrix composites. Therefore, when micro and nano scale particles coexist in HAMCs, the DRX behavior and nucleation mechanism will be more complex in the thermal forming process, due to the influence of SiC_p at different scales on the DRX behavior of composites.

Until now, there have been few reports about the DRX behavior of HAMCs in the available literature. Consequently, in the present study, based on the stress–strain curves and the relationship of the work hardening rate-strain of dual-scale SiC_p/A356 composites, the critical strain model and kinetic model of DRX were determined to describe the DRX behaviors of HAMCs. Meanwhile, the microstructure evolution of the studied composites was explored by electron back-scattered diffraction (EBSD) and transmission electron microscopy (TEM). The DRX behavior and nucleation mechanism were investigated. It provides significant data support for improving the microstructure and comprehensive performance of HAMCs accurately.

2 Experimental materials and procedures

The material used in this experiment was A356 composites reinforced with dual-scale SiC_p . One scale of SiC_p was 10 μ m with a fraction of 23 vol%, and the other was 80 nm with a fraction of 2 vol%. The matrix material was A356 alloy powders with a mean size of 7 μ m, and the chemical compositions of the A356 alloy are listed in Table 1.

Figure 1 displays the fabrication process of the composites used. The A356 powders were mixed with nanosized SiC_p by the high-energy ball milling for 12 h with a rotation speed of 150 rpm and a ball-to-powder weight ratio of 8:1, and then the pre-prepared composite powders were mixed with micro-sized SiC_p using the same process. After that, an LDJ 200/600-300 YS cold isostatic pressing equipment was employed to press the mixed powders with a 240 MPa pressure for 15 s, and then the cold-pressed specimens were sintered in a VAF-7720 furnace with 2×10^{-2} Pa at 550°C for 4 h. The specimens were hot extruded by an XJ-500 type extruder at 500°C. The extrusion ratio was 15:1, and the speed was 1 mm/s. At last, the bars were annealed at 300°C for 2 h.

Morphologies of the composites were observed using a ZEISS EVO 18 scanning electron microscopy (SEM) operated at 20 kV and a JEOL JEM-2100 transmission electron microscope (TEM) operated at 200 kV. The samples for TEM observation were thin foils with a diameter of 3 mm and thickness of about 50 μm, which were twinjet electropolished in a 75% methanol and 25% nitric acid solution at about –30°C. Figure 2a–e reveals the microstructure of raw material powders and mixed powders. The microstructures of the studied composites are shown in Figure 2f–h. Obviously, micro-SiC_p are uniformly distributed in the Al matrix (Figure 2f). Meanwhile, no agglomerations of nano-SiC_p are observed (Figure 2g).

The hot compressed samples with a length of 12 mm and a diameter of 8 mm were prepared. The hot deformation was tested at temperatures of $460-520^{\circ}$ C and strain rates of $0.01-5 \, \text{s}^{-1}$ by a Gleeble-1500D thermal simulation

Table 1: The chemical compositions of the A356 alloy used

Element	Si	Mg	Cu	Fe	Al
Weight percent (wt%)	7.0	0.3	0.1	0.1	Bal.

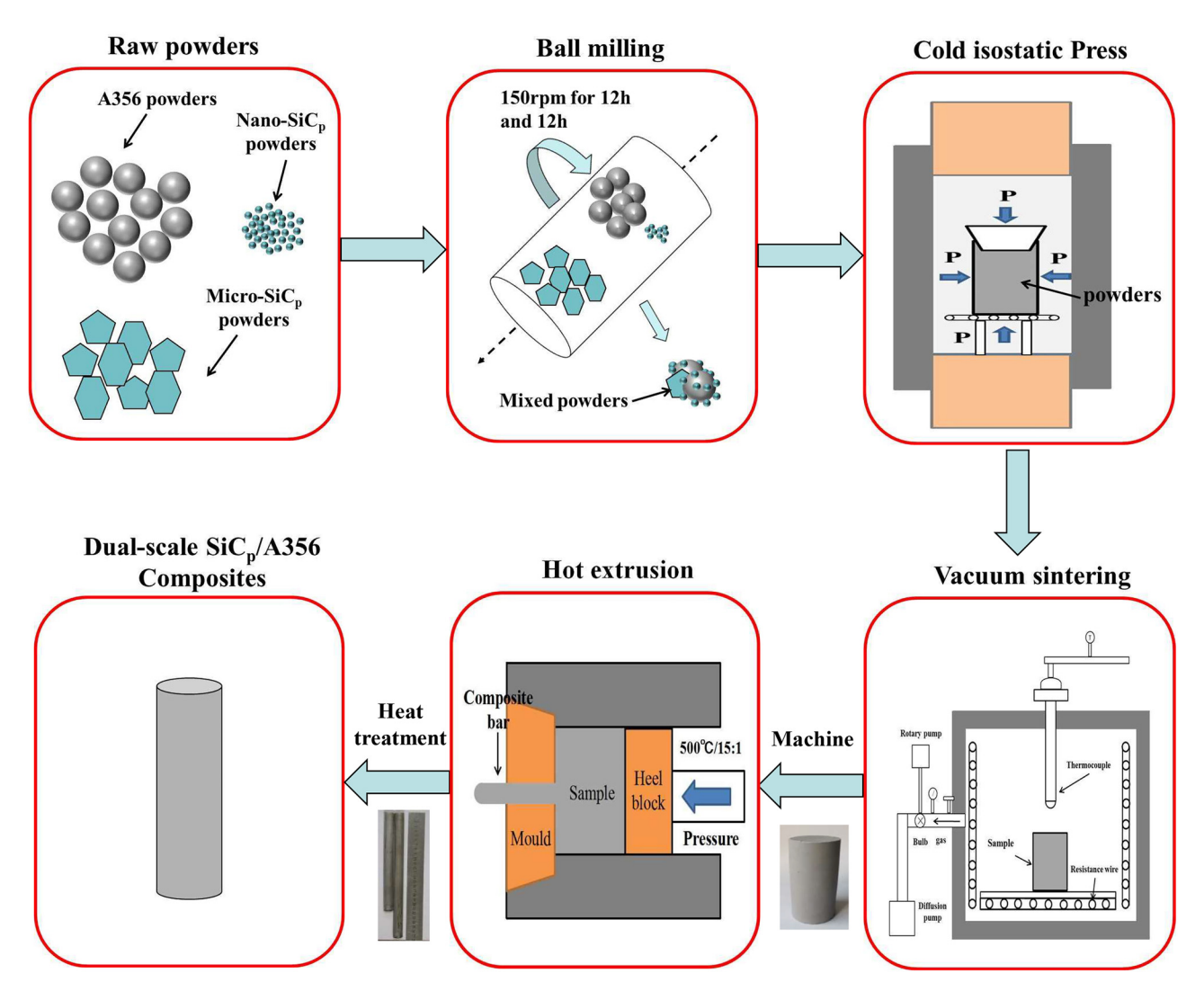


Figure 1: The fabrication process of dual-scale SiC_p/A356 composites used.

DE GRUYTER

tester. The true strain was 0.7 in the trial. The schematic diagram of the hot compression process is shown in Figure 3. In addition, to analyze the microstructure evolution of the composites during thermal deformation, compression specimens with the true strains of 0.1, 0.3, and 0.5 at the temperature of 500°C and strain rate of $1 \, \mathrm{s}^{-1}$ were water quenched immediately. The microstructures of the compressed specimens were analyzed by EBSD and TEM. EBSD images were tested by the JMS-7800F field emission SEM operated at 20 kV. The EBSD data were analyzed by the Transmission Channel 5 software. The samples for EBSD measurements were electro-polished using 25 vol% HNO3 in methanol at 20°C and 5 V, and then the observation surface was carried out in a Precision ion polishing system.

Results and discussion

3.1 True stress-strain curves

The true stress-strain curves of the used composites under different deformation conditions are presented in Figure 4. The temperatures and strain rates significantly affect the flow stress of the HAMCs. The curves show typical DRX characteristics with single peak stress [21]. During the hot deformation process, with the increase in the strain, the true stress rapidly reaches a peak value due to the work hardening. It then decreases slowly owing to the dynamic recovery (DRV) and DRX.

The peak stress of the composites used under various deformation conditions is displayed in Figure 5. The peak

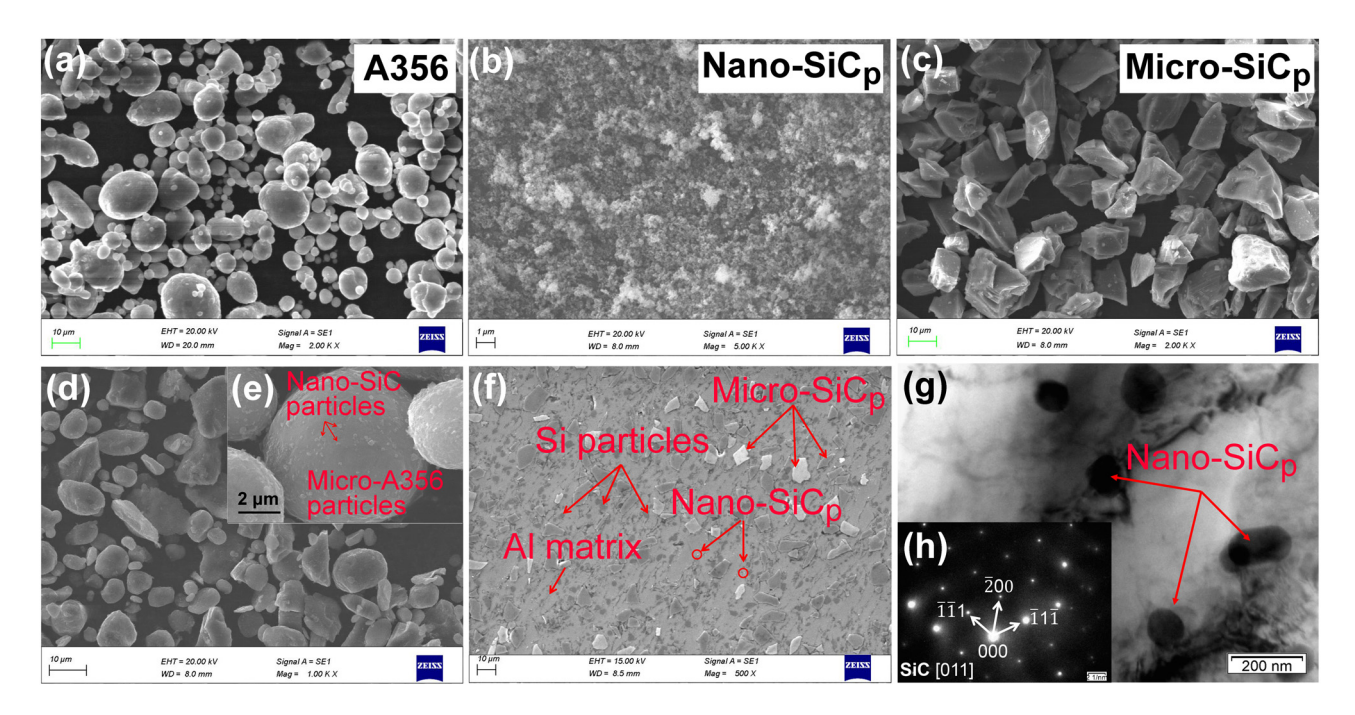


Figure 2: Morphologies of the preparation process of dual-scale $SiC_p/A356$ composites used: (a) A356 powders; (b) nano- SiC_p powders; (c) micro- SiC_p powders; (d) mixed powders after ball milling; (e) high-magnification image of the mixed powders showing the uniform distribution of nano- SiC_p on the A356 particles; (f) SEM images of the composites; (g) TEM images of the composites; and (h) corresponding diffraction pattern of the nano- SiC_p .

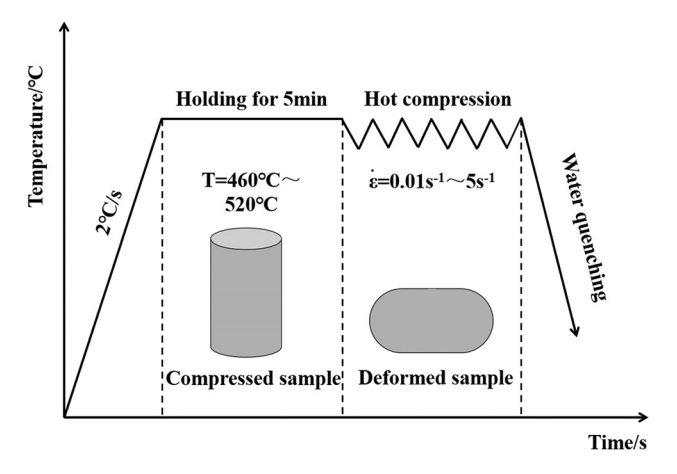


Figure 3: Schematic diagram of the hot compression process.

stress decreases as the temperature increases. It indicates that the composites are sensitive to the deformation temperatures, which is similar to that of single-scale micro or nano-SiC $_p$ /Al composites as reported in refs [22,23]. It is attributed to the stronger dynamic softening at high temperatures. Figure 5 also demonstrates that the peak stress increases with the strain rate at the same temperature. Because of the increased strain rate, the time for the deformation structure nucleation and growth is insufficient, and the dislocation multiplication increases rapidly. It is

evident that work hardening occurs, suggesting that the flow stress increases. Thus, the composites studied have a positive sensitivity to strain rate.

3.2 Constitutive equation

For the hot deformation behavior of AMCS, the equations (1)–(3) are generally employed to demonstrate the relationship between the strain rate $(\dot{\varepsilon})$, deformation temperature (T), and flow stress (σ) [24–26]. Besides, as a temperature-compensated strain rate factor, the Zener–Holloman parameter (Z) can be used to describe the combined effects of the temperature and strain rate during the hot deformation process, which is expressed using equation (4) [24].

$$\dot{\varepsilon} = A_1 \sigma^{n'} \exp\left(\frac{-Q}{RT}\right), \quad (\alpha \sigma \le 0.8),$$
 (1)

$$\dot{\varepsilon} = A_2 \exp(\beta \sigma) \exp\left(\frac{-Q}{RT}\right), \quad (\alpha \sigma \ge 1.2),$$
 (2)

$$\dot{\varepsilon} = A[\sinh(\alpha\sigma)]^n \exp\left(\frac{-Q}{RT}\right), \quad (\text{for all } \sigma),$$
 (3)

$$Z = \dot{\varepsilon} \exp\left(\frac{-Q}{RT}\right) = A[\sinh(\alpha\sigma)]^n, \qquad (4)$$

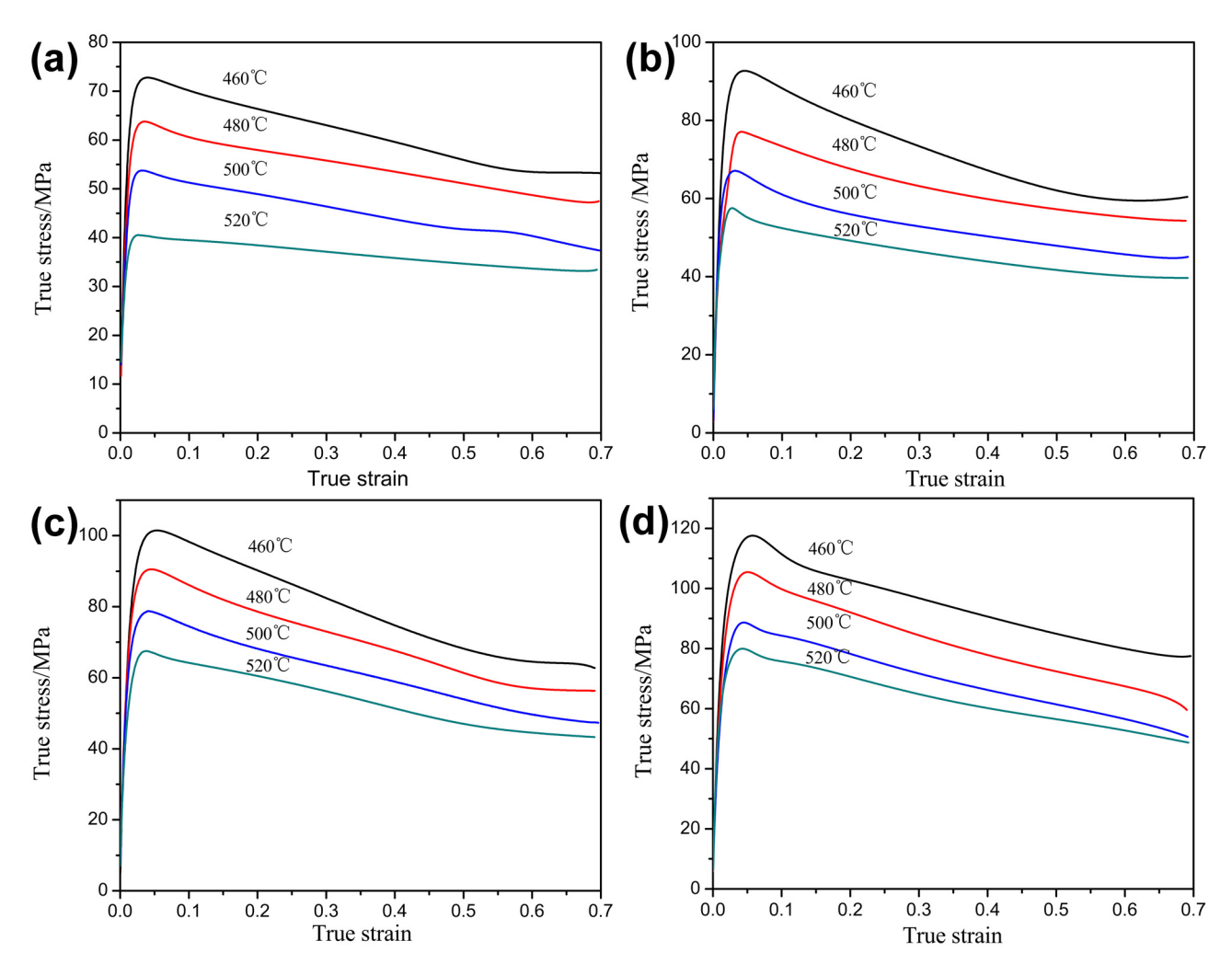


Figure 4: The true stress–strain curves at different strain rates: (a) $\dot{\varepsilon} = 0.01 \, \text{s}^{-1}$; (b) $\dot{\varepsilon} = 0.1 \, \text{s}^{-1}$; (c) $\dot{\varepsilon} = 1 \, \text{s}^{-1}$; and (d) $\dot{\varepsilon} = 5 \, \text{s}^{-1}$.

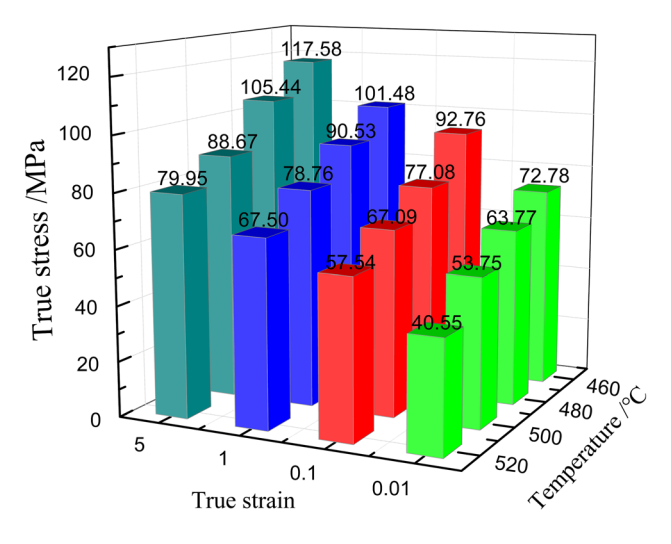


Figure 5: Peak stress under different deformation conditions.

where A_1 , A_2 , A, α , n, β , and n' are constant ($\alpha = \beta/n'$); R, T, and Q stand for the gas constant (8.314 J/mol K), deformation temperature (K), and deformation activation energy (kJ/mol), respectively.

Taking the natural logarithms on both sides for equations (1)–(4), we get

$$\ln \dot{\varepsilon} = \ln A_1 + n' \ln \sigma - \frac{Q}{RT}, \tag{5}$$

$$\ln \dot{\varepsilon} = \ln A_2 + \beta \sigma - \frac{Q}{RT},\tag{6}$$

$$\ln \dot{\varepsilon} = \ln A + n \ln[\sinh(\alpha \sigma)] - \frac{Q}{RT}, \tag{7}$$

$$\ln Z = \ln \dot{\varepsilon} + Q/RT = \ln A + n \ln[\sinh(\alpha \sigma)]. \tag{8}$$

Substituting the peak stress and corresponding strain rate values in equations (5) and (6). Scatter diagrams and

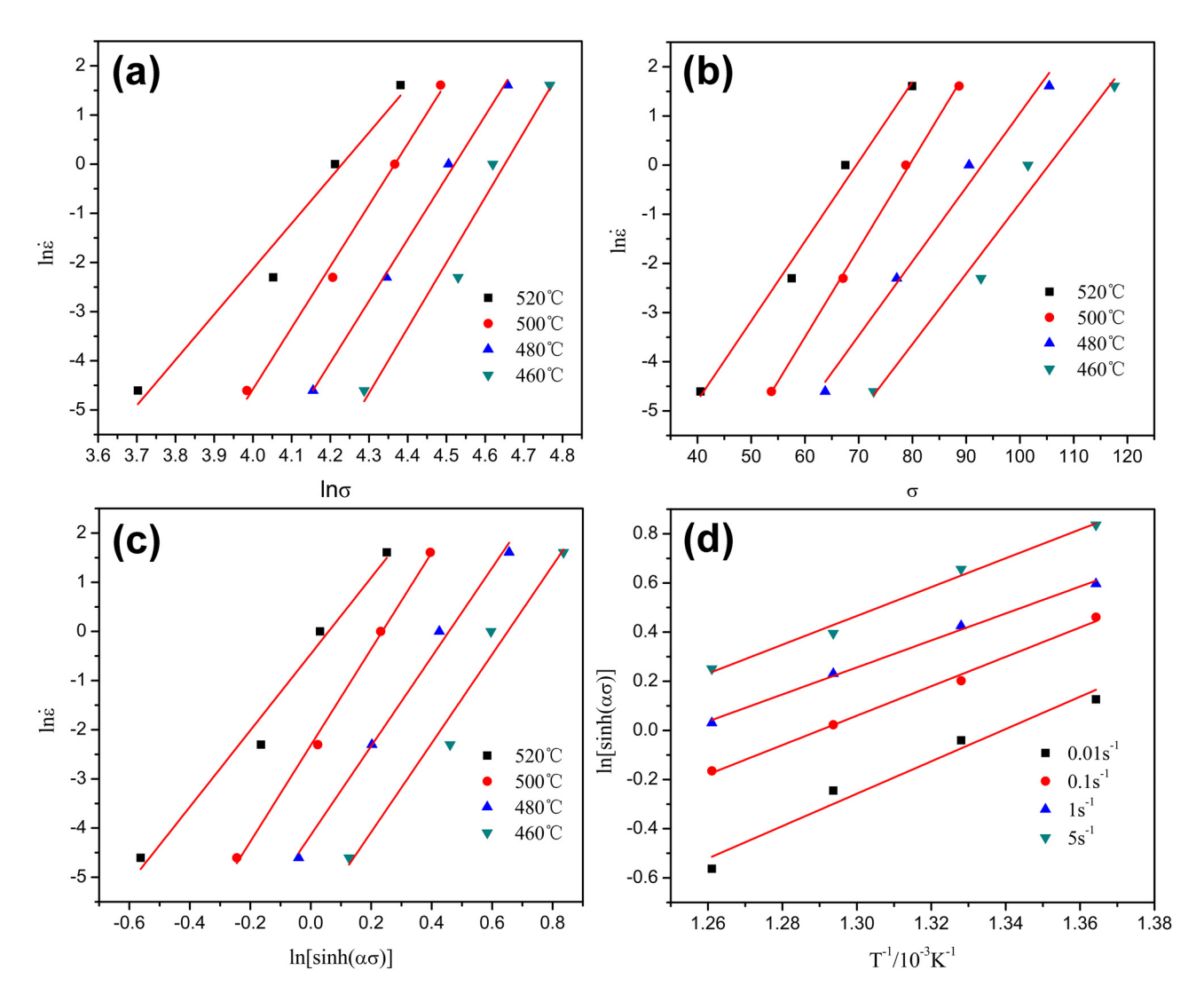


Figure 6: Scatter diagrams and linear regression fits: (a) $\ln \sigma - \ln \dot{\epsilon}$; (b) $\sigma - \ln \dot{\epsilon}$; (c) $\ln [\sinh(\alpha \sigma)] - \ln \dot{\epsilon}$; and (d) $T^{-1}/10^{-3}K^{-1} - \ln [\sinh(\alpha \sigma)]$.

linear regression fits of the $\ln \sigma - \ln \dot{\varepsilon}$, $\sigma - \ln \dot{\varepsilon}$, $\ln[\sinh(\alpha\sigma)] - \ln \dot{\varepsilon}$, and $T^{-1}/10^{-3}K^{-1} - \ln[\sinh(\alpha\sigma)]$ are shown in Figure 6. By calculating the average slopes of various fitting lines (Figure 6a and b), n' and β can be obtained to be 11.88984 and 0.15909, respectively. Therefore, this gives a value of $\alpha = \beta/n' = 0.01338$.

According to equation (7), Q can be obtained from equation (9).

$$Q = R \frac{\partial \ln \left[\sinh(\alpha \sigma) \right]}{\partial (1/T)} \left|_{\dot{\varepsilon}} \cdot \frac{\partial \ln \dot{\varepsilon}}{\partial \ln \sinh(\alpha \sigma)} \right|_{T} = nRK, \quad (9)$$

where n and K are the slopes of $\ln \dot{\varepsilon} - \ln[\sinh(\alpha \sigma)]$ and $\ln[\sinh(\alpha \sigma)] - 1,000/T$ curves. According to equation (7), their calculated results are 8.9168 and 5.9784 (Figure 6c and d), respectively. Using equation (9), the value of Q can be calculated as 443.204 kJ/mol.

Table 2: The values of $\ln Z$ under different deformation conditions

$\dot{\varepsilon}$ (s ⁻¹)			(°C)	
	460	480	500	520
0.01	68.12082028	66.18918707	64.35750900	62.61822327
0.1	70.42340537	68.49177216	66.66009409	64.92080836
1	72.72599047	70.79435725	68.96267919	67.22339346
5	74.33542838	72.40379516	70.57211710	68.83283137

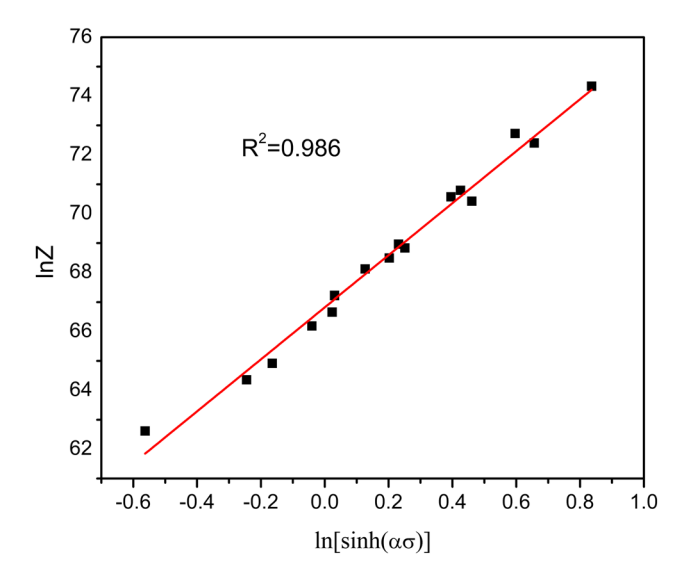


Figure 7: The relationship between the peak stress and *Z* parameter.

According to equation (8) and Q value, the values of $\ln Z$ under the different T and $\dot{\varepsilon}$ are summarized in Table 2. $\ln Z$ and $\ln[\sinh(\alpha\sigma)]$ exhibit a linear relationship determined by Figure 7 with a correlation coefficient of 0.986, meaning that all σ values in equation (3) are reliable. Moreover, the $\ln Z$ value increases gradually with the decrease in deformation temperatures or the increase in strain rates, which is like the evolution characteristic of peak stress. Therefore, the Z parameter synthesizes the hot deformation conditions of materials, representing the relationship between flow stress, deformation temperature, and strain rate during hot deformation.

3.3 The critical strain for DRX

In general, the appearance of peak stress in stress–strain curves of a material suggests that DRX occurs. Moreover,

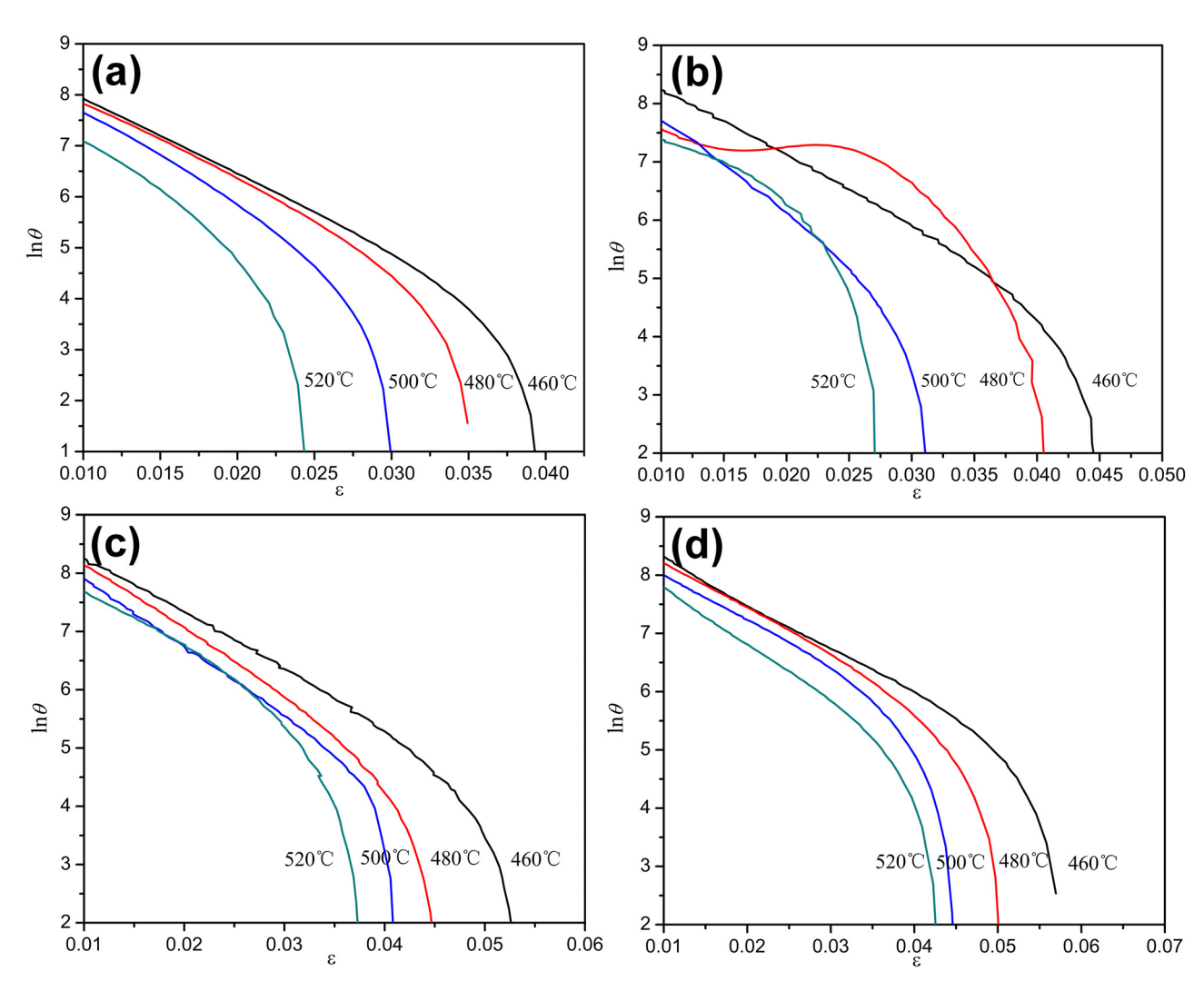


Figure 8: The relationship curves between $\ln \theta$ and ε under different deformation conditions; (a) $\dot{\varepsilon} = 0.01 \, \text{s}^{-1}$; (b) $\dot{\varepsilon} = 0.1 \, \text{s}^{-1}$; (c) $\dot{\varepsilon} = 1 \, \text{s}^{-1}$; and (d) $\dot{\varepsilon} = 5 \, \text{s}^{-1}$.

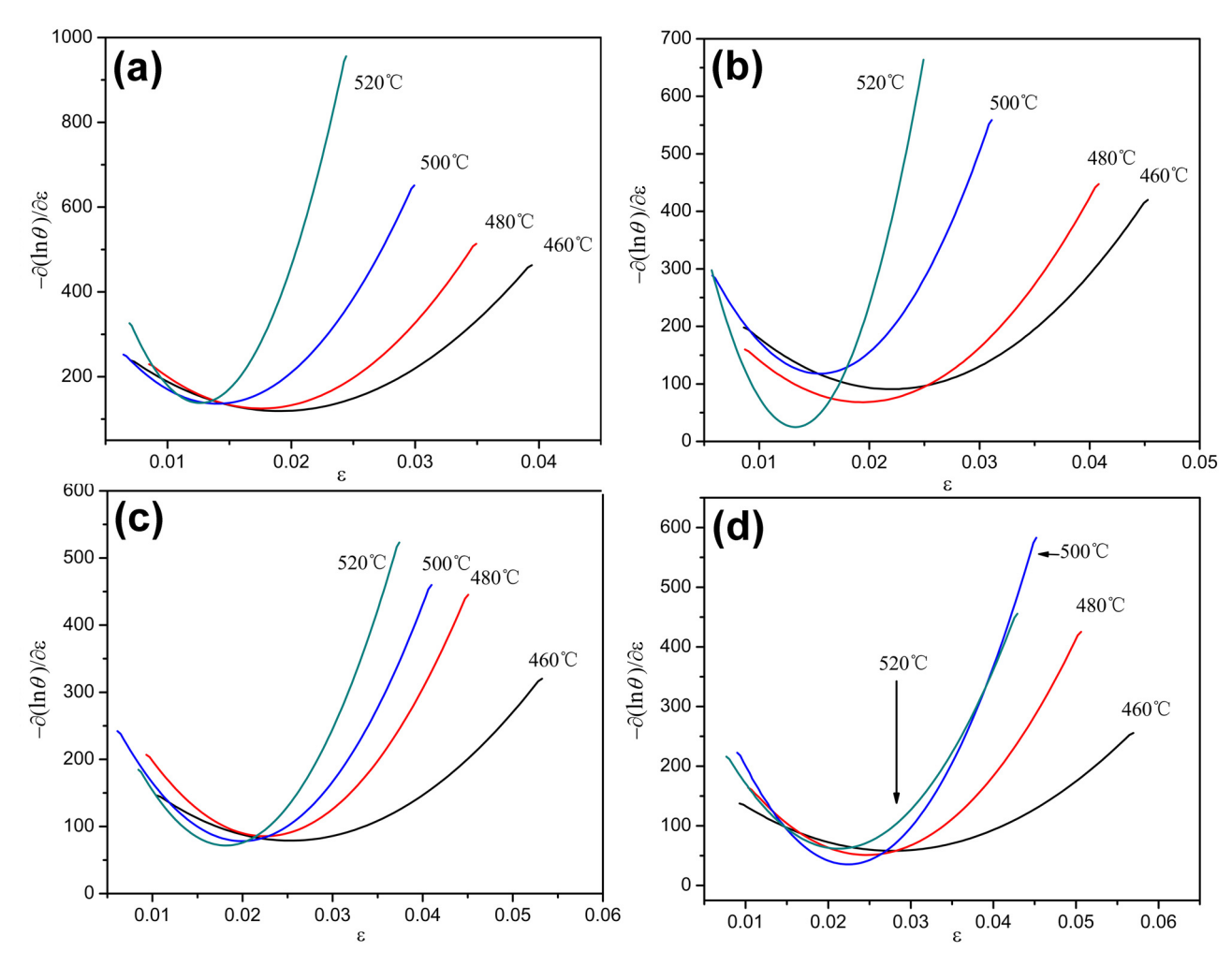


Figure 9: The relationship curves between $-\delta(\ln \theta)/\delta \varepsilon$ and ε under different deformation conditions: (a) $\dot{\varepsilon} = 0.01 \, \text{s}^{-1}$; (b) $\dot{\varepsilon} = 0.1 \, \text{s}^{-1}$; (c) $\dot{\varepsilon} = 1 \, \text{s}^{-1}$; and (d) $\dot{\varepsilon} = 5 \, \text{s}^{-1}$.

Table 3: Critical strain (ϵ_c) and peak strain (ϵ_p) of DRX under different deformation conditions

$\dot{\varepsilon}$ (s ⁻¹)	Parameter	<i>T</i> (°C)				
		460	480	500	520	
0.01	\mathcal{E}_{c}	0.01911	0.01757	0.01446	0.01265	
	$\boldsymbol{arepsilon}_{ extsf{p}}$	0.03942	0.03548	0.03048	0.02597	
0.1	$\boldsymbol{\varepsilon}_{c}$	0.02198	0.01915	0.0155	0.01328	
	$oldsymbol{arepsilon}_{p}$	0.04529	0.04083	0.03111	0.02715	
1	$oldsymbol{arepsilon}_{c}$	0.02496	0.0225	0.01995	0.01815	
	$oldsymbol{arepsilon}_{p}$	0.05325	0.04505	0.04095	0.0374	
5	$oldsymbol{arepsilon}_{c}$	0.02781	0.02467	0.0224	0.02128	
	$oldsymbol{arepsilon}_{p}$	0.05785	0.05062	0.0452	0.0429	

the DRX has occurred before it reaches the peak strain. Therefore, the determination of critical strain has a great significance on the hot working process [27,28]. The work hardening rate-flow stress (θ – σ) curves may be employed

to describe the microstructure evolution of materials during hot deformation [29]. Meanwhile, the work hardening rate is defined as $\theta = \partial \sigma/\partial \varepsilon$. Based on the approach of Poliak and Jonas [30], the $\theta-\sigma$ curve shows a distinct inflection point, which is described as $-\partial^2\theta/\partial\sigma=0$. The inflection points of $\theta-\sigma$ curves indicate the initiation of DRX. According to the relationship of partial derivatives, $-\partial(\ln\theta)/\partial\varepsilon=\partial\theta/\partial\sigma$ equation can be deduced. It suggests that the curves of $\ln\theta-\varepsilon$ also render corresponding inflection point features [31]. Therefore, according to the stress–strain curves, the $\ln\theta-\varepsilon$ and $-\partial(\ln\theta)/\partial\varepsilon-\varepsilon$ curves can be obtained. Then, the corresponding critical strain value $(\varepsilon_{\rm c})$ can be directly acquired by the minimum value of the $-\partial(\ln\theta)/\partial\varepsilon-\varepsilon$ curves.

Figure 8 presents the relationship curves between $\ln \theta$ and ε of the composites used under various deformation conditions. The curves of $\ln \theta - \varepsilon$ show a similar trend. The variation law of the work hardening rate

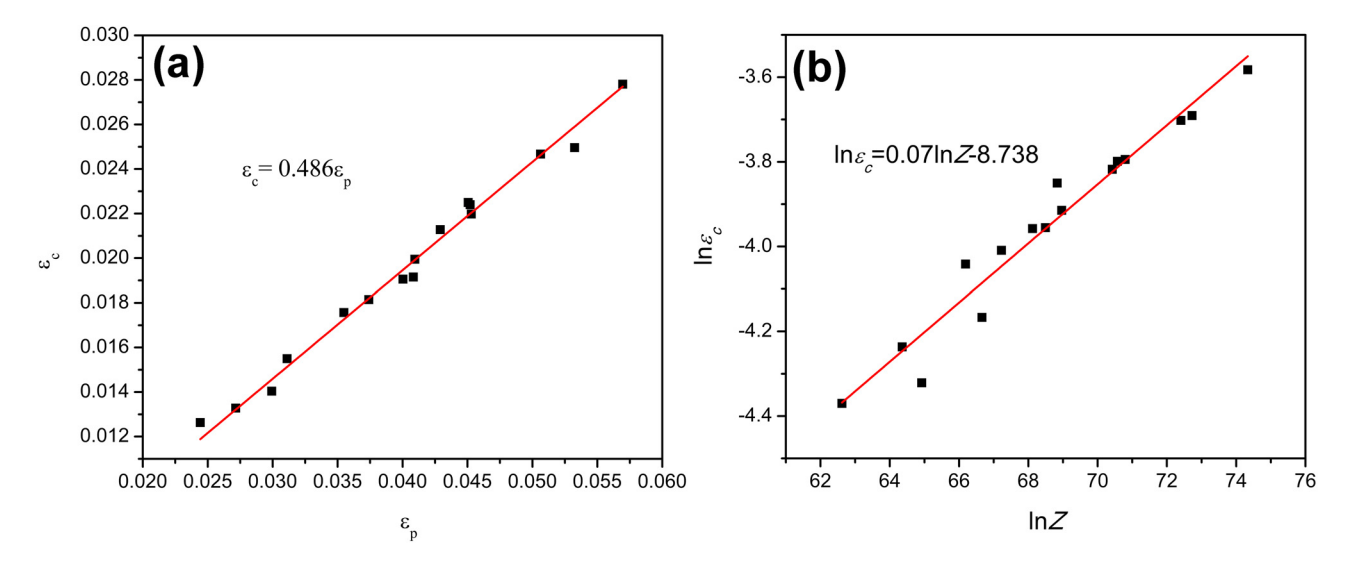


Figure 10: Relationship of (a) $\varepsilon_c - \varepsilon_p$ and (b) $\ln \varepsilon_c - \ln Z$.

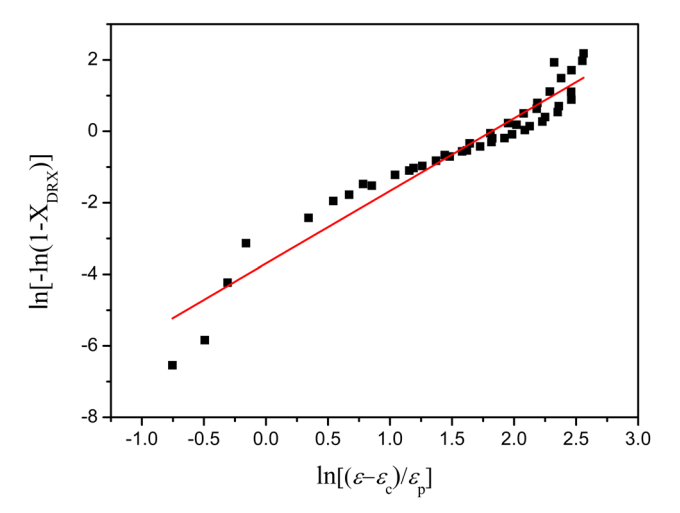


Figure 11: Relationship between $ln[-ln(1 - X_{DRX})]$ and $ln[(\varepsilon - \varepsilon_c)/\varepsilon_p]$.

decreases quickly with the increase in strain, then decreases slowly, and finally enters a rapidly decreasing stage again. Meanwhile, the inflection point can be obtained at the corresponding strain place.

The relationship curves between $-\partial(\ln\theta)/\partial\epsilon$ and ϵ under various deformation conditions are displayed in Figure 9. With the increase in strain, the values of $-\partial(\ln\theta)/\partial\epsilon$ gradually decrease, and then slowly rise after the minimum values appear. The minimum value of the $-\partial(\ln\theta)/\partial\epsilon-\epsilon$ curve corresponds to the critical strain causing DRX. Combining with the peak strain in Figure 4, the vital strains and peak strain under various deformation conditions can be captured, which are listed in Table 3.

The critical model of DRX proposed by Sellars *et al*. [26] is used to demonstrate the influence of temperatures

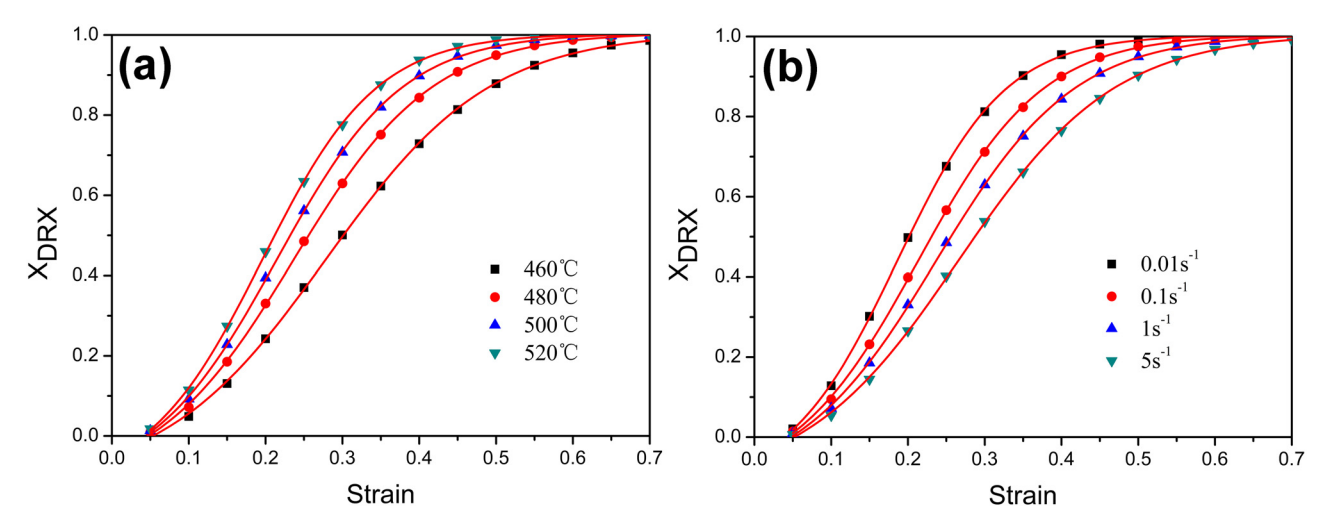


Figure 12: The relationship curves between X_{DRX} and the strain based on equation (11): (a) $\dot{\varepsilon} = 1 \, \text{s}^{-1}$ and (b) $T = 500^{\circ}\text{C}$.

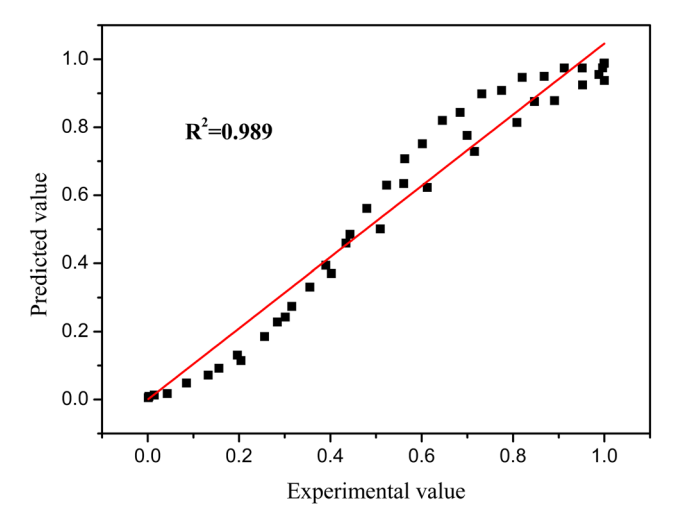


Figure 13: Experimental and predicted values of DRX volume fraction.

and strain rates on the essential strain of DRX in the present work. The equation can be described as follows:

$$\varepsilon_{\rm c} = k\varepsilon_{\rm p},$$
 (10)

$$\varepsilon_{\rm c} = aZ^{\rm b},$$
 (11)

where k, a, and b are constants, ε_c , ε_p , and Z are critical strain, peak strain, and Zener–Hollomon parameter, respectively. According to the data in Table 3, there is a certain relationship between the critical strain and peak strain of DRX. As shown in Figure 10a, the ratio of the two $(\varepsilon_c/\varepsilon_p)$ is 0.486. Based on the critical strain values and their corresponding Z values under different deformation conditions, the relationship diagram of $\ln \varepsilon_c - \ln Z$ is drawn, as shown in Figure 10b. Obviously, there is an ideal linear relationship between $\ln \varepsilon_c$ and $\ln Z$ by linear fitting. Therefore, the critical strain model for DRX can be expressed as follows: $\varepsilon_c = 1.604 \times 10^{-4} Z^{0.07}$.

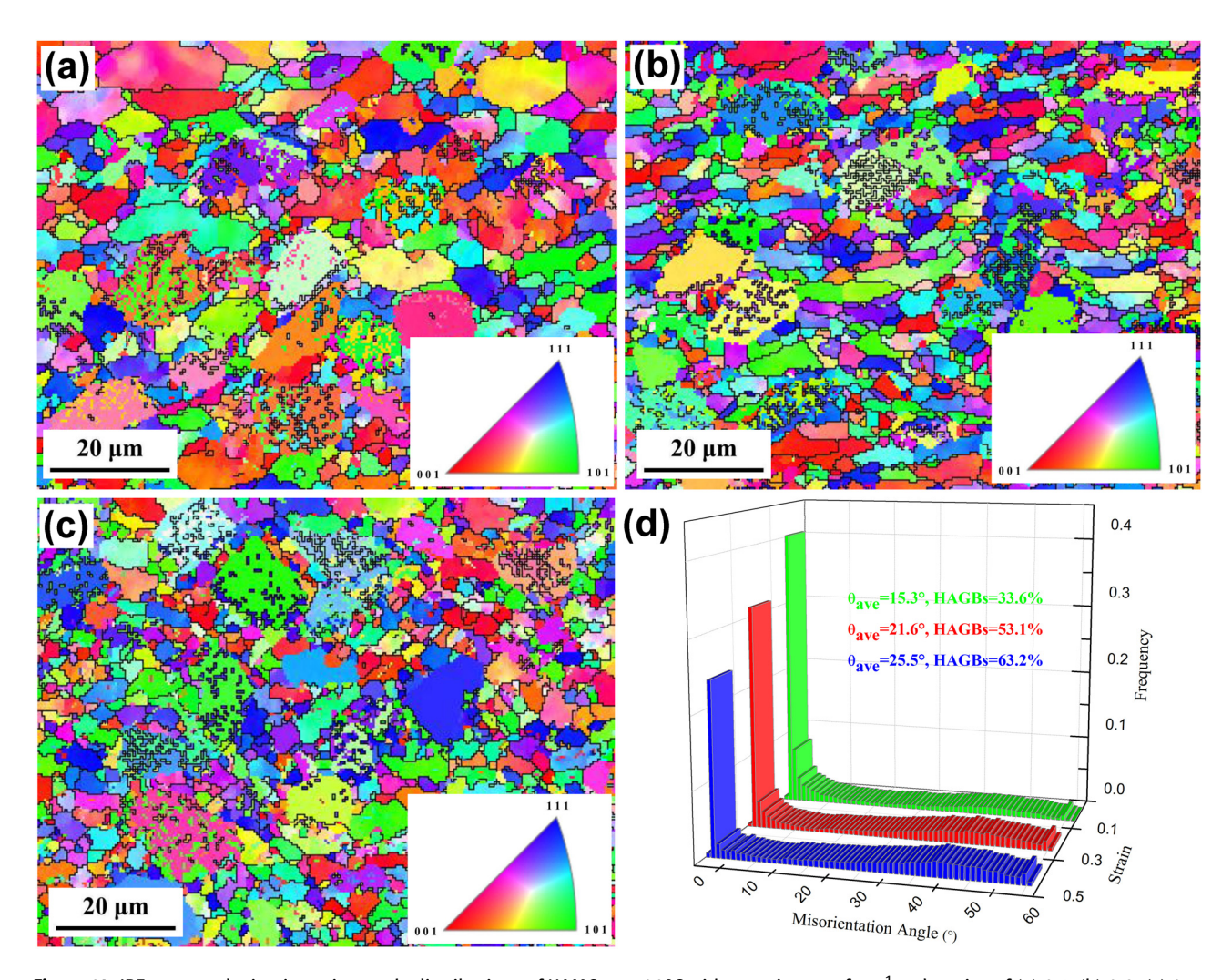


Figure 14: IPF maps and misorientation angle distributions of HAMCs at 500° C with a strain rate of $1 \, \text{s}^{-1}$ and strains of (a) 0.1, (b) 0.3, (c) 0.5, and (d) misorientation angle distributions in (a-c).

According to the above analysis, the peak strain lags behind the critical strain, meaning that DRX occurs prior to the peak strain. The increase in *Z* value will lead to the increase in the critical strain, which is a disadvantage for the occurrence of DRX. Therefore, increasing the deformation temperature and reducing the strain rate will be a large favor to the microstructure uniformity and grain refinement, which will also improve the comprehensive properties of the materials.

3.4 DRX kinetic model

It can be seen from Figure 4 that DRX is the most important softening mechanism of the studied composites. Because of the important role of DRX in improving the plastic formability and performance of materials, it is an effective approach to explore the deformation mechanism

of the composites by constructing DRX kinetic model. At present, the most widely used DRX dynamic model is the Johnson–Mehl–Avrami (JMA) equation [32,33].

$$X_{\rm DRX} = 1 - \exp \left[-B \left(\frac{\varepsilon - \varepsilon_{\rm c}}{\varepsilon_{\rm p}} \right)^m \right],$$
 (12)

where $X_{\rm DRX}$ is the DRX volume fraction; B and m are constants; ε is the true strain; $\varepsilon_{\rm c}$ and $\varepsilon_{\rm p}$ represent the critical strain and peak strain of DRX, respectively. It is well known that the softening behavior of DRX can effectively reduce the flow stress during hot deformation. Accordingly, the $X_{\rm DRX}$ can be calculated based on the characteristic stress value in the flow stress curves, which can be represented as follows [34]:

$$X_{\rm DRX} = \frac{\sigma_{\rm p} - \sigma}{\sigma_{\rm p} - \sigma_{\rm ss}},\tag{13}$$

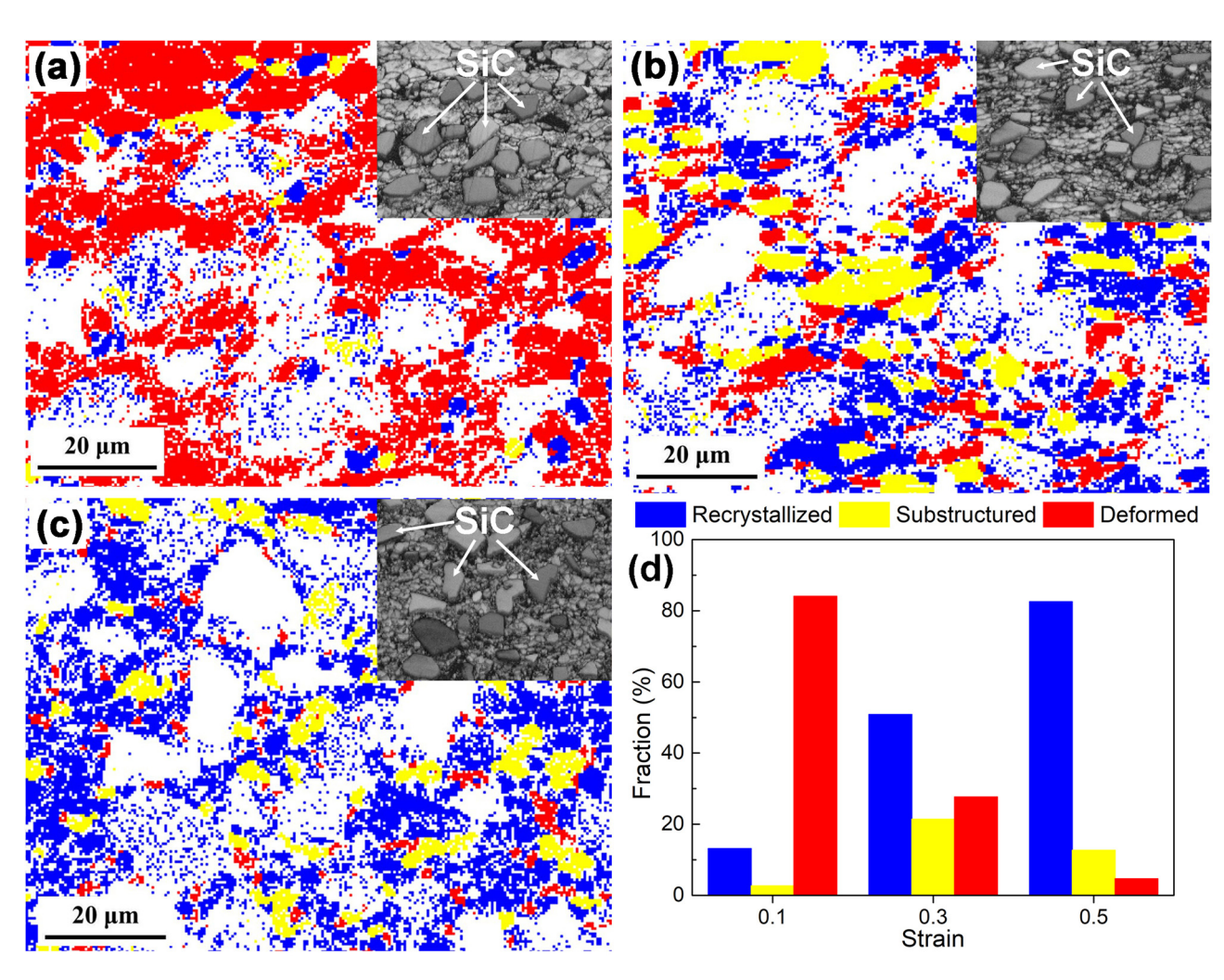


Figure 15: EBSD maps of HAMCs at 500°C with a strain rate of $1 \, \text{s}^{-1}$ and strains of (a) 0.1, (b) 0.3, (c) 0.5, and (d) fractions of three types of microstructures in (a-c).

where σ , σ_p , and σ_{ss} are the transient stress, peak stress, and steady-state stress, respectively. Equation (14) can be expressed by taking the natural logarithms on both sides of equation (12).

$$\ln[-\ln(1 - X_{DRX})] = \ln B + m \ln \left[\frac{\varepsilon - \varepsilon_{c}}{\varepsilon_{p}}\right]. \quad (14)$$

According to equation (14), linear regression is performed for $\ln[(\varepsilon - \varepsilon_c)/\varepsilon_p]$ and $\ln[-\ln(1 - X_{DRX})]$, as shown in Figure 11. Therefore, the values of B and m can be obtained to be 0.0248 and 2.0306, respectively. By substituting B and m in equation (12), the DRX kinetic model of the composites can be described as follows:

$$X_{\rm DRX} = 1 - \exp \left[-0.0248 \left(\frac{\varepsilon - \varepsilon_{\rm c}}{\varepsilon_{\rm p}} \right)^{2.0306} \right].$$
 (15)

Figure 12 displays the relationship curves of $X_{\rm DRX}$ and strain under various deformation conditions. It can be found that the curves are similar and present the characteristics of S-type curves. In the initial stage of deformation, $X_{\rm DRX}$ grows at a relatively low rate and then increases rapidly. After reaching a certain value, $X_{\rm DRX}$ tends to grow slowly. Additionally, when the strain remains constant, $X_{\rm DRX}$ increases with the increase in the deformation temperatures and decrease in the strain rates.

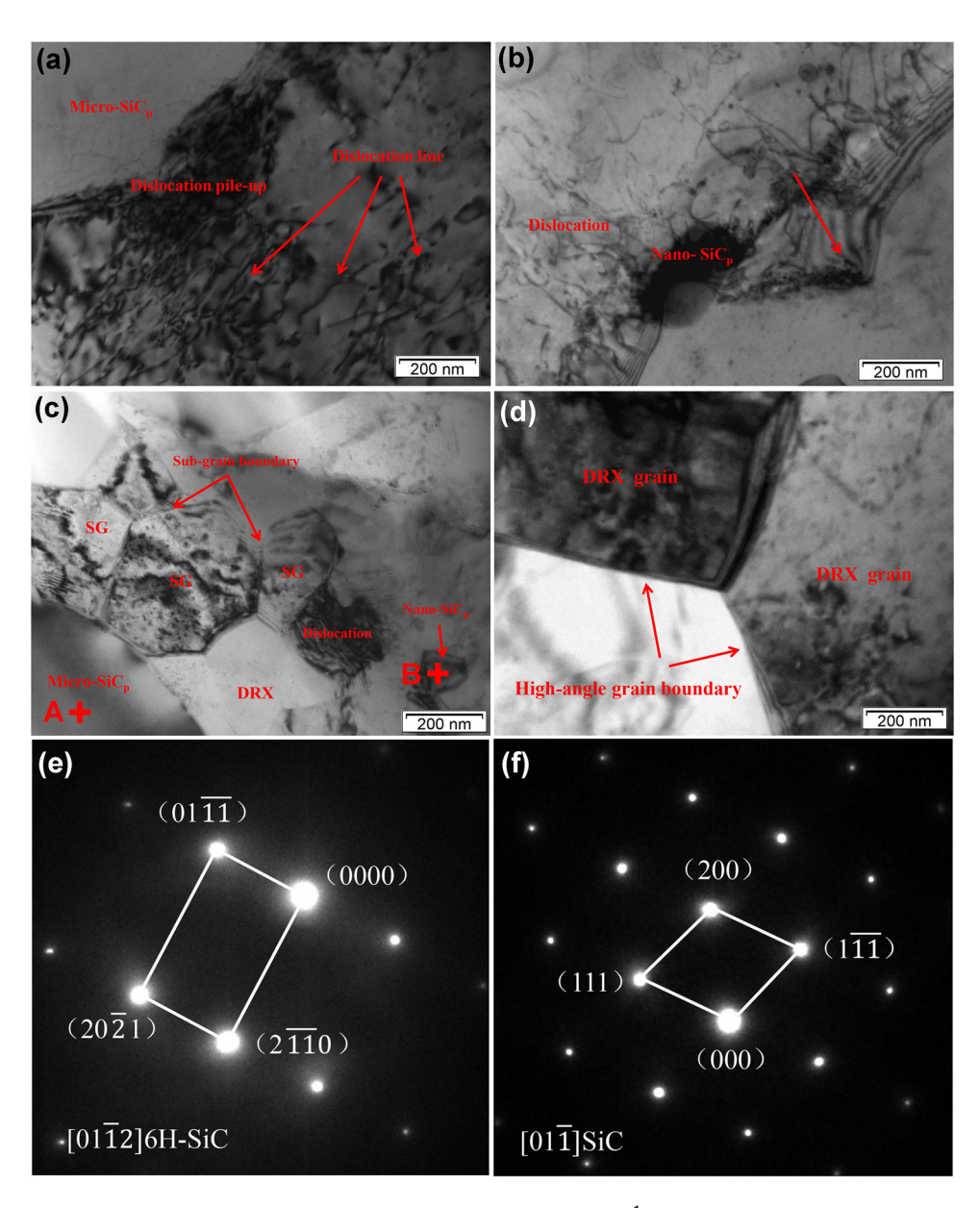


Figure 16: TEM microstructures of the HAMCs at different strains ($T = 500^{\circ}$ C, $\dot{\varepsilon} = 1 \, \text{s}^{-1}$): (a) and (b) $\varepsilon = 0.1$; (c) $\varepsilon = 0.3$; (d) $\varepsilon = 0.5$; (e) and (f) are selected-area electron diffraction patterns of particles A and B in (c), respectively.

To verify the accuracy of the DRX kinetic model, the experimental values measured are regressed linearly with the predicted values calculated by the model, and the fitting precision is 0.989 (Figure 13). It means that the $X_{\rm DRX}$ of the composites can be well predicted by the kinetic model.

3.5 Microstructure evolution

Figure 14 displays the inverse pole figure (IPF) maps and misorientation angle distributions of the used composites at the temperature of 500°C, strain rate of 1 s⁻¹, and strain of 0.1, 0.3, and 0.5. In the initial deformation stage, the original grain boundaries bulge and form a sawtooth shape (Figure 14a). With the increase in strain, the grain morphology of HACMs changes obviously. The initial grains are flattened or elongated, resulting in a color

gradient between adjacent sub-grains in the slender grain (Figure 14b). With the further increase in strain, many fine equiaxed DRX grains are formed, and their orientation is obviously different from their adjacent grains (Figure 14c).

Additionally, it can be seen from misorientation angle distributions (Figure 14d), with the increase in strain, that the proportion of high-angle grain boundaries (HAGBs) is 33.6, 53.1, and 63.2%, respectively. This result illustrates that with the increase in strain, the HAGBs always increase, and the low-angle grain boundaries (LAGBs) gradually transform into HAGBs. Therefore, the increase in strain will promote the continuous migration from LAGBs to HAGBs, resulting in a higher recrystallization degree [35]. This is also consistent with the prediction trend of the DRX kinetic model.

Figure 15 shows the EBSD images of the HAMCs after hot deformation. Blue color represents recrystallized,

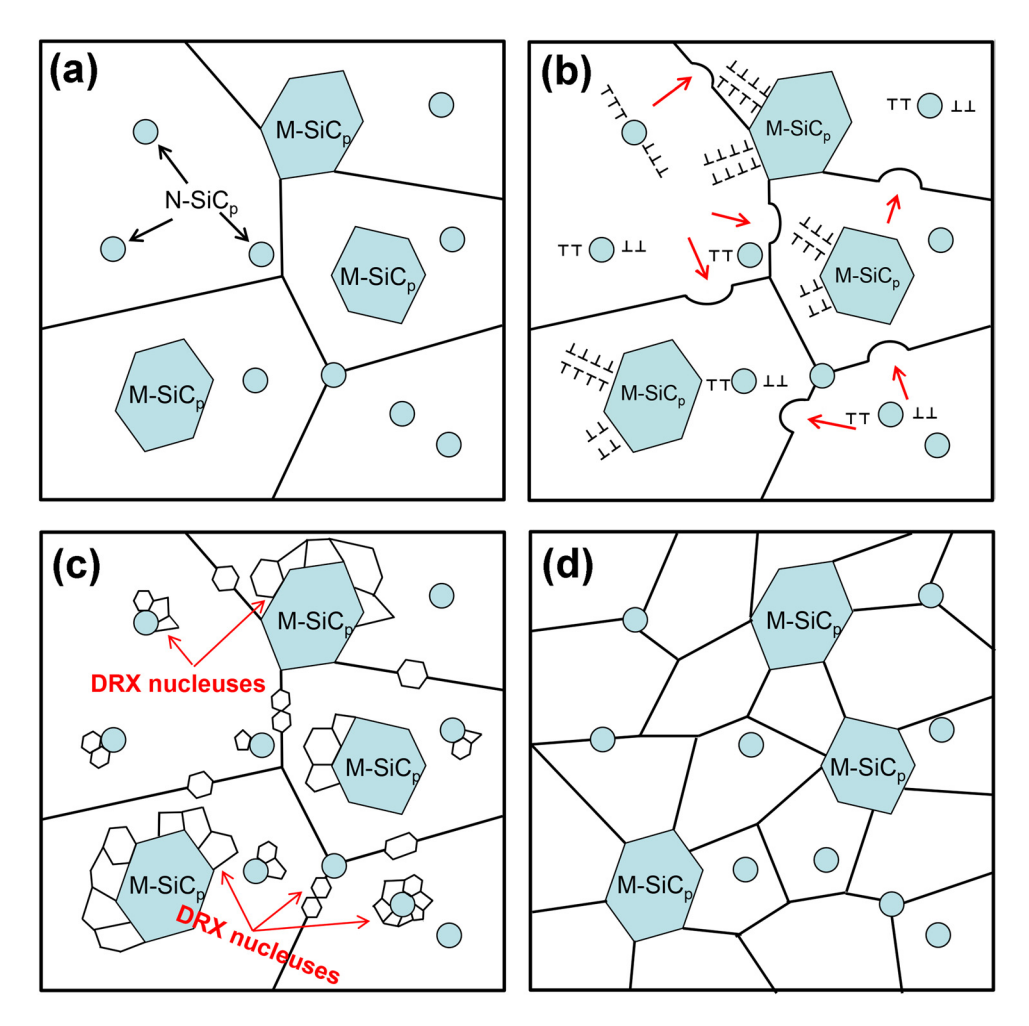


Figure 17: Schematic illustration of microstructure evolution mechanism of the used composites during hot deformation: (a) initial microstructure; (b) dislocations pile-up around reinforced particles and grain boundary bulging; (c) DRX nucleuses around grain boundaries and reinforcing particles; and (d) microstructure after deformation.

yellow color represents substructure, and red color represents deformed in Figure 15d. It confirms that the DRX occurs during the deformation. The proportion of $X_{\rm DRX}$ in Figure 15(a–c) are 13.2, 50.9, and 82.6%, respectively. The $X_{\rm DRX}$ gradually increases with the strain. Although there is a certain gap between the actual detection results and the theoretical calculation value through the DRX kinetic model (Figure 12), the overall change trend is consistent, which further verifies the applicability of the DRX kinetic model.

To further explore the DRX behavior of the composites, the microstructures of different strains are investigated by TEM, as shown in Figure 16. At the beginning of hot deformation ($\varepsilon = 0.1$), severe dislocation accumulation occurs around the particles, owing to the deformation mismatch between the SiC particles and Al matrix. Thus, high-density dislocations can be easily found in the deformed grains (Figure 16a). At the same time, the deformed grain boundaries are uneven, and the original grain boundaries bulge as marked using the red arrow in Figure 16b. With the increase in strain ($\varepsilon = 0.3$), dislocations gather near grain boundaries and particles through climbing and crossing slip, and obvious sub-grain structures are formed. The sub-grain boundaries are clear and have the trend of merging and combination-grow up (Figure 16c). With the further increase in strain ($\varepsilon = 0.5$), the sub-grain boundaries gradually transform into grain boundaries with the clear and sharp large angles through merging and rotation. Finally, the new recrystallized grains occur, and the dislocations inside the grain basically disappear (Figure 16d). According to the results of these microstructural observations, the primary softening mechanism of the HACMs is DRX during hot deformation obviously [36–38]. However, there is a difference about the softening mechanism of the HACMs reported in ref. [39]. Their results indicate that the dominant softening mechanism of Al-Si/(SiC_p + TiB₂) HAMCs is DRV, accompanied by partial DRX. This may be related to the thermal deformation parameters and the content of reinforcing particles.

According to the above observation and analysis, Figure 17 depicts the microstructure evolution mechanism of the composites in the DRX process. In the initial stage of hot deformation, high density and orientation gradient deformation zones appear near the micro-SiC $_p$ due to deformation mismatch between the Al matrix and these particles. Besides, dense dislocations can also be found around the nano-SiC $_p$ owing to the pinning effect of these particles [40,41]. So many dislocations will occur around these micro-SiC $_p$ and nano-SiC $_p$ particles. At the same time, the original grain boundaries bulge because of the

strain (Figure 17b). When the dislocation accumulation and proliferation in the material reach a certain degree, DRX will preferentially nucleate around grain boundaries and reinforcing particles as the strain increases (Figure 17c). With the further increase in strain, the misorientation angle of new DRX grains gradually increases due to the accumulation and reorganization of dislocations. Then, the LAGBs can be transformed into the HAGBs. Finally, uniform and fine equiaxed grains are formed due to the pinning impact of nano-SiC_p (Figure 17d). In conclusion, the DRX mechanism of the studied composites mainly consists of grain boundary bulging mechanism, PSN mechanism, and sub-grain rotation induced nucleation mechanism. With the increase in strain, the DRX characteristics of subgrain rotation and combination-grow up were further revealed [42,43].

Furthermore, it indicates that both micro-SiC_p and nano-SiC_p can facilitate the DRX nucleation of the aluminum matrix in the PSN mechanism. The existence of micro-SiC_p plays a primary role in stimulating the DRX nucleation by forming the particle deformation zone (PDZ) [16]. However, PDZ by nano-SiC_p is relatively small, which has a minor impact on DRX nucleation. The addition of nano-SiC_p increases the dislocation density in the Al matrix continuously, resulting in the dislocations pile-up, thereby stimulating DRX nucleation. Thus, the dual-scale particles both play a role in promoting DRX nucleation of the HACMs. Meanwhile, the pinning effect of nanoparticles on grain boundaries leads to grain refinement. Similar behavior has been reported in SiC_p reinforced Mg matrix composites [44].

4 Conclusion

The hot compression tests of dual-scale $SiC_p/A356$ matrix composites were performed under different deformation conditions. DRX behavior and mechanisms were carefully investigated. The main conclusions are summarized as follows:

- The stress-strain curves show typical DRX characteristics with single peak stress. The comprehensive influences of the strain rate and deformation temperature on the stress are investigated using the *Z* parameter, in which the deformation activation energy is 443.204 kJ/mol.
- 2) The critical strain causing DRX is obtained by the inflection of $\ln\theta \varepsilon$. The relationship between the critical strain and peak strain is described as $\varepsilon_c = 0.486\varepsilon_p$. Furthermore, the model for the critical strain of DRX is determined as $\varepsilon_c = 1.604 \times 10^{-4} Z^{0.07}$.

3) Based on the stress-strain curve data, the DRX kinetic model of composites can be constructed by the classical Avrami equation as follows:

DE GRUYTER

$$X_{\text{DRX}} = 1 - \exp \left[-0.0248 \left(\frac{\varepsilon - \varepsilon_{\text{c}}}{\varepsilon_{\text{p}}} \right)^{2.0306} \right]$$

4) The dominant softening mechanism of dual-scale SiC_p/A356 composites during the hot deformation is the DRX mechanism, which includes grain boundaries bulging mechanism, particle stimulated nucleation mechanism, and sub-grain rotation induced nucleation mechanism. Both micro-SiC $_{\! \rm p}$ and nano-SiC $_{\! \rm p}$ can stimulate the DRX nucleation of the Al matrix because of the PSN mechanism.

Funding information: The authors acknowledge the financial support from the National Natural Science Foundation of China (Grant No. 52171138).

Author contributions: Yahu Song: methodology, investigation, and writing - original draft. Aigin Wang: supervision and writing - review and editing. Douqin Ma: writing – review and editing. Jingpei Xie: writing – review and editing. Wenyan Wang: writing -review and editing. All authors have accepted responsibility for the entire content of this manuscript and approved its submission.

Conflict of interest: The authors state no conflict of interest.

Data availability statement: The raw/processed data required to reproduce these findings cannot be shared at this time as the data also form part of an ongoing study.

References

- Wu C, Gao T, Liu X. In situ SiC reinforced Si-SiC 3D skeletons in SiC/Al-Si composites. J Alloy Compd. 2019;810:151730.
- Yuan D, Yang X, Wu S, Lü S, Hu K. Development of high strength and toughness nano-SiC_p/A356 composites with ultrasonic vibration and squeeze casting. J Mater Process Tech. 2019;269:1-9.
- Lakshmikanthan A, Bontha S, Krishna M, Koppad PG, Ramprabhu T. Microstructure, mechanical and wear properties of the A357 composites reinforced with dual-sized SiC particles. J Alloy Compd. 2019;786:570-80.
- Chen HS, Wang WX, Nie HH, Zhou J, Li YL, Liu RF, et al. Microstructure evolution and mechanical properties of B₄C/ 6061Al neutron absorber composite sheets fabricated by powder metallurgy. J Alloy Compd. 2018;730:342-51.

- Steinman AE, Corthay S, Firestein KL, Kvashnin DG, Kovalskii AM, Matveev AT, et al. Al-based composites reinforced with AlB2, AlN and BN phases: Experimental and theoretical studies. Mater Des. 2018;141:88-98.
- Mousavian RT, Behnamfard S, Khosroshahi RA, Zavašnik J, Ghosh P, Krishnamurthy S, et al. Strength-ductility trade-off via SiC nanoparticle dispersion in A356 aluminium matrix. Mater Sci Eng A. 2020;771:138639.
- Dong X, Wang A, Xie J, Wang Z. Optimization of volume fraction and microstructure evolution during thermal deformation of nano-SiC_p/Al-7Si composites. Nanotechnol Rev. 2021;10:1306-17.
- Zhang LJ, Qiu F, Wang JG, Wang HY, Jiang QC. Microstructures and mechanical properties of the Al2014 composites reinforced with bimodal sized SiC particles. Mater Sci Eng A. 2015;637:70-4.
- [9] Tian WS, Zhao QL, Geng R, Qiu F, Jiang QC. Improved creep resistance of Al-Cu alloy matrix composite reinforced with bimodal-sized TiC_n. Mater Sci Eng A. 2018;713:190-4.
- [10] Tan A, Teng J, Zeng X, Fu D, Zhang H. Fabrication of aluminium matrix hybrid composites reinforced with SiC microparticles and TiB2 nanoparticles by powder metallurgy. Powder Metall. 2017;60(1):66-72.
- Jahedi M, Mani B, Shakoorian S, Pourkhorshid E, Hossein Paydar M. Deformation rate effect on the microstructure and mechanical properties of $Al-SiC_p$ composites consolidated by hot extrusion. Mater Sci Eng A. 2012;556:23-30.
- Srivastava VC, Jindal V, Uhlenwinkel V, Bauckhage K. Hotdeformation behavior spray-formed 2014 Al + SiCp metal matrix composites. Mater Sci Eng A. 2008;477:86-95.
- [13] Zhang P, Li F. Dynamic recrystallization model of SiC particle reinforced aluminum matrix composites. Rare Met Mater Eng. 2010;39(7):1166-70.
- [14] Sun Y, Xie J, Hao S, Wang A, Liu P, Li M. Dynamic recrystallization model of 30% SiC_p/Al composite. J Alloy Compd. 2015;649:865-71.
- Doherty RD, Hughes, DA, Humphreys, FJ, Hughes DA, Humphreys FJ, Jonas JJ, Jensen D, Kassner ME, et al. Current issues in recrystallization: a review. Mater Sci Eng A. 1997;238:219-74.
- [16] Humphreys FJ. The nucleation of recrystallization at second phase particles in deformed aluminium. Acta Metall. 1977;25(11):1323-44.
- [17] Chan HM, Humphreys FJ. The recrystallization of Aluminum-Silicon alloys containing a bimodal particle distribution. Acta Mater. 1984;32:235-43.
- [18] Wu Y, Yu Y, Zhang Q, Zhu T, Zhai R, Zhao X. Hot deformation behavior and processing map of in situ nano ZrB2 reinforced AA6111 matrix composites. Mater Res Exp. 2019;6(2):026528.
- [19] Kai X, Zhao Y, Wang A, Wang C, Mao Z. Hot deformation behavior of in situ nano ZrB2 reinforced 2024Al matrix composite. Compos Sci Technol. 2015;116:1-8.
- [20] Radi Y, Mahmudi R. Effect of Al₂O₃ nano-particles on the microstructural stability of AZ31 Mg alloy after equal channel angular pressing. Mater Sci Eng A. 2010;527:2764-71.
- Wei H, Liu G, Xiao X, Zhang M. Dynamic recrystallization [21] behavior of a medium carbon vanadium microalloyed steel. Mater Sci Eng A. 2013;573:215-21.
- [22] Mcgueen HJ, Myshlyaev M, Konopleva E. High temperature mechanical and microstructural behavior of A356/15 vol% SiC_p and A356 alloy. Can Metall Quart. 2013;37(2):125-39.

- [23] Wang Z, Wang A, Xie J, Liu P. Hot deformation behavior and strain-compensated constitutive equation of nano-sized SiC particle-reinforced Al-Si matrix composites. Materials. 2020;13(8):1812.
- [24] Zener C, Hollomon JH. Effect of strain rate upon plastic flow of steel. J Appl Phys. 1944;15(1):22–32.
- [25] Wang Y, Ling DL, Law CC. A correlation between tensile flow stress and Zener-Hollomon factor in TiAl alloys at high temperatures. J Mater Sci Lett. 2000;19(13):1185–8.
- [26] Sellars CM, Mc WJ, Tegart G. Hot workability. Int Metall Rev. 1972;17:1–24.
- [27] Li B, Chu ZJ, Du Y, Zhou W, Zhou X. Hot deformation behavior and dynamic recrystallization kinetics of a novel Sc and Zr modified ultra-high-strength Al-Zn-Mg-Cu alloy. J Mater Eng Perform. 2020;29(12):7774–84.
- [28] Zhang H, Chen G, Chen Q, Han F, Zhao Z. A physically-based constitutive modelling of a high strength aluminum alloy at hot working conditions. J Alloy Compd. 2018;743:283–93.
- [29] Zambrano OA, Logé RE. Dynamic recrystallization study of a Fe-Mn-Si based shape memory alloy in constant and variable thermo mechanical conditions. Mater Charact. 2019;152:151–61.
- [30] Poliak El, Jonas JJ. A one-parameter approach to determining the critical conditions for the initiation of dynamic recrystallization. Acta Mater. 1996;44(1):127–36.
- [31] Rouzegar R, Azadbeh M, Danninger H. High-temperature flow behaviour modelling of stress-strain curves of the sintered Cu-28Zn pre-alloyed powder compacts considering dynamic recrystallisation. Powder Metall. 2017;61(2):1-7.
- [32] Jonas JJ, Quelennec X, Jiang L, Martin É. The Avrami kinetics of dynamic recrystallization. Acta Mater. 2009;57:2748-56.
- [33] Wen DX, Lin YC, Zhou Y. A new dynamic recrystallization kinetics model for a Nb containing Ni-Fe-Cr-base super alloy considering influences of initial δ phase. Vacuum. 2017;141:316–27.
- [34] Chen MS, Yuan WQ, Lin YC, Li HB, Zou ZH. Modeling and simulation of dynamic recrystallization behavior for 42CrMo steel by an extended cellular automaton method. Vacuum. 2017;146:142–51.

- [35] Lin YC, Wu XY, Chen XM, Chen J, Wen DX, Zhang JL, et al. EBSD study of a hot deformed nickel-based super alloy. J Alloy Compd. 2015;640:101–13.
- [36] Wang Y, Zhao G, Xu X, Chen X, Zhang C. Constitutive modeling, processing map establishment and microstructure analysis of spray deposited Al-Cu-Li alloy 2195. J Alloy Compd. 2019;779:735-51.
- [37] Sun ZC, Wu HL, Cao J, Yin ZK. Modeling of continuous dynamic recrystallization of Al-Zn-Cu-Mg alloy during hot deformation based on the internal-state-variable (ISV) method. Int J Plast. 2018:106:73-87.
- [38] Luo L, Liu Z, Bai S, Zhao J, Zeng D, Wang J, et al. Hot deformation behavior considering strain effects and recrystallization mechanism of an Al-Zn-Mg-Cu alloy. Materials. 2020;13(7):1743.
- [39] Chen X, Fu D, Teng J, Zhang H. Hot deformation behavior and mechanism of hybrid aluminum-matrix composites reinforced with micro-SiC and nano-TiB₂. J Alloy Compd. 2018:753:566-75.
- [40] Robson JD, Henry DT, Davis B. Particle effects on recrystallization in magnesium-manganese alloys: Particle-stimulated nucleation. Acta Mater. 2009;57(9):2739-47.
- [41] Deng K, Shi J, Wang C, Wang X, Wu Y, Nie K, et al. Microstructure and strengthening mechanism of bimodal size particle reinforced magnesium matrix composite. Compos Part A. 2012;43(8):1280-4.
- [42] Sun ZC, Zheng LS, Yang H. Softening mechanism and microstructure evolution of as-extruded 7075 aluminum alloy during hot deformation. Mater Charact. 2014;90:71–80.
- [43] Chen K, Tang J, Jiang F, Teng J, Fu D, Zhang H. The role of various Zr additions in static softening behavior of Al-Zn-Mg-Cu alloys during interval holding of double-stage hot deformation. J Alloy Compd. 2019;792:1112-21.
- [44] Wang CJ, Deng KK, Zhou SS, Liang W. Dynamic recrystallization behavior of bimodal size SiC_p reinforced Mg matrix composite during hot deformation. Acta Metall Sin (Engl Lett). 2016;29(6):527–37.